nature physics

LETTERS

https://doi.org/10.1038/s41567-020-0983-9

Check for updates

Suppression of superconductivity by anisotropic strain near a nematic quantum critical point

Paul Malinowski[1], Qianni Jiang[1], Joshua J. Sanchez[1], Joshua Mutch[1], Zhaoyu Liu[1], Preston Went[1], Jian Liu[2], Philip J. Ryan[3,4], Jong-Woo Kim[3] and Jiun-Haw Chu[1]✉

In most unconventional and high-temperature superconductors, superconductivity emerges as a nearby symmetry-breaking phase is suppressed by chemical doping or pressure[1–7]. This has led to the belief that the fluctuations associated with the symmetry-breaking phase are beneficial, if not responsible, for the superconducting pairing[8,9]. A direct test to verify this hypothesis is to observe a decrease of the superconducting critical temperature (T_c) by applying the symmetry-breaking conjugate field that suppresses the dynamic fluctuations of the competing order. However, most of the competing phases in unconventional superconductors break translational symmetry, requiring a spatially modulated conjugate field that is difficult to realize experimentally. Here, we show that anisotropic strain, the conjugate field of nematicity, reduces the T_c of an iron pnictide. For optimally doped samples we show a fivefold reduction of T_c with less than one per cent of strain. For underdoped samples, T_c becomes zero yielding a fully metallic ground state. In addition to providing direct evidence of the role played by the nematic fluctuations in the formation of the superconducting state, these results demonstrate tunable mechanical control of a high-temperature superconductor, an important step forward for technological applications of superconductivity.

The electronic nematic phase[10] found in the iron-based superconductors is a rare example of a wave-vector $\mathbf{q}=0$ competing phase proximate to unconventional superconductivity, in that it only breaks the crystalline four-fold rotational symmetry in the B_{2g} symmetry channel. In the iron pnictides a collinear antiferromagnetic order further breaks translational and time-reversal symmetries within the nematic phase[11,12], whereas in the iron chalcogenides nematic order may exist without long-range magnetic order[13,14]. Owing to the finite electron–lattice coupling, the nematicity induces an orthorhombic structural distortion that can be considered as a secondary order parameter. X-ray diffraction measurements have shown a suppression of the orthorhombic distortion upon entering the superconducting state[15], which is direct evidence of the competition between the nematic and superconducting phases. Above the nematic phase transition, the orthorhombic lattice distortion induced by uniaxial stress plays the role of the conjugate field of the primary nematic order parameter. One application of this idea is the measurement of the bare nematic susceptibility, in which the induced electronic anisotropy is measured above the phase transition under a constant anisotropic strain[16–19]. The divergence of this bare nematic susceptibility demonstrates unambiguously that the structural transition is electronically driven[20]. Notably, a diverging nematic susceptibility is observed in a wide range of optimally doped iron-based superconductors, suggesting the correlation of optimal T_c with nematic quantum critical fluctuations[21].

Here we investigate the effect of B_{2g} anisotropic strain on the superconducting transition in $Ba(Fe_{1-x}Co_x)_2As_2$ through electrical transport, magnetic susceptibility and X-ray diffraction measurements. Resistivity measurements were performed as a function of temperature and applied uniaxial stress, with current flowing parallel to the direction of the applied stress along the Fe–Fe bonding direction. In this configuration the uniaxial stress induces a B_{2g} anisotropic strain that couples linearly to nematicity. We used a strain cell (Supplementary Fig. 1) capable of applying large, tunable uniaxial stress at low temperatures[22]. The uniaxial stress is controlled by the displacement of two strain cell plates across which the sample is mounted. The relative change of the size of the gap between the plates, ε_{disp}, was measured by resistive strain gauges, and corresponds to a tensile (compressive) uniaxial stress for positive (negative) values. Nevertheless, ε_{disp} is distinct from the actual lattice distortion due to the imperfect strain transmission and the formation of twin domains in the underdoped samples. The actual lattice distortion was either measured directly by X-ray diffraction or calculated by finite-element simulations (see Methods and Supplementary Fig. 2).

We focus first on the $x=0.042$ composition that lies in the underdoped region of the phase diagram (Fig. 1a). With decreasing temperature, the free-standing sample undergoes nematic (structural), magnetic and superconducting phase transitions at $T=75$ K, 67 K and 13 K, respectively (Fig. 1b). Thus, the application of uniaxial stress is expected to enhance an orthorhombicity that is already present at zero stress due to the nematic transition. The resistivity as a function of temperature under different applied stress is shown in Fig. 1c–f. Inspection of these data shows that for small ε_{disp}, the value of the resistivity above the superconducting transition changes rapidly while the superconducting transition temperature changes little. In this range of ε_{disp} the only effect of uniaxial stress is to align nematic domains without changing the lattice constants, and the strong modulation of resistivity is due to the large resistance anisotropy associated with the orthorhombic phase[23,24]. Then for $\varepsilon_{disp} > 2.7\times10^{-3}$ and $\varepsilon_{disp} < 0.9\times10^{-3}$, at which point the sample is fully detwinned and the crystal lattice is further distorted by the uniaxial stress, the superconducting transition is dramatically suppressed for both compressive (Fig. 1c) and tensile (Fig. 1d) stress. The effect of the stress on the superconducting transition is even more striking when the resistivity is shown on a logarithmic

[1]Department of Physics, University of Washington, Seattle, WA, USA. [2]Department of Physics and Astronomy, University of Tennessee, Knoxville, TN, USA. [3]Advanced Photon Source, Argonne National Laboratories, Lemont, IL, USA. [4]School of Physical Sciences, Dublin City University, Dublin, Ireland. ✉e-mail: jhchu@uw.edu

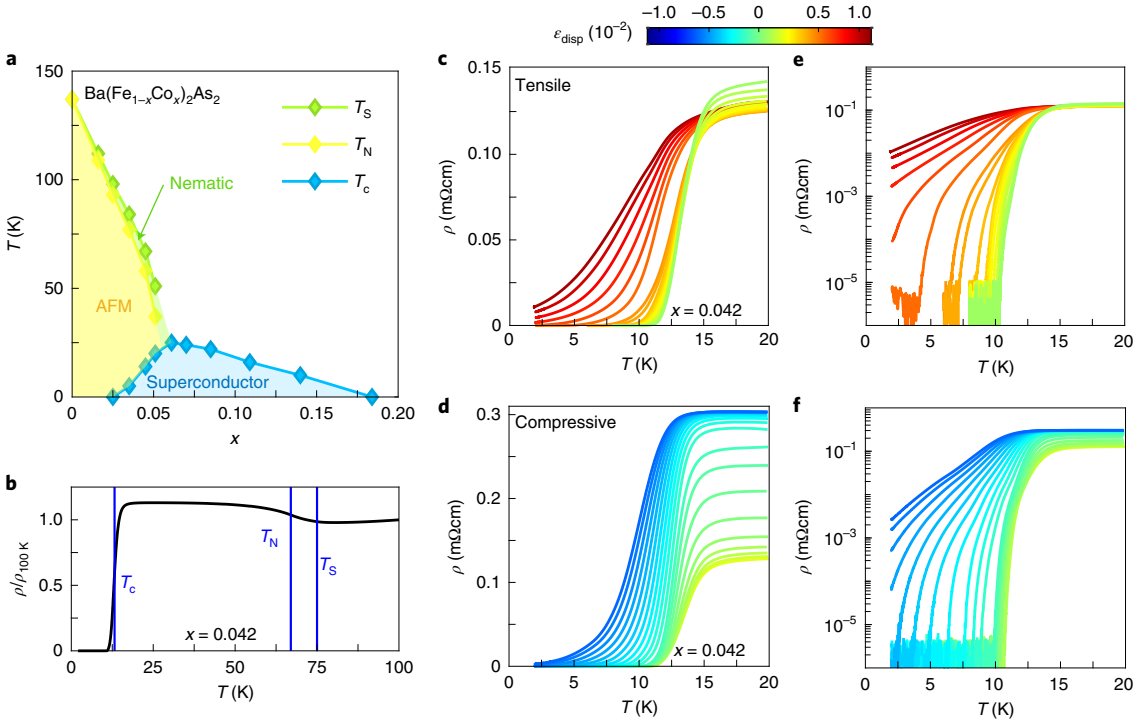

Fig. 1 | Background and superconducting transition in $Ba(Fe_{0.958}Co_{0.042})_2As_2$ under uniaxial stress. a, Temperature–composition phase diagram[11] of $Ba(Fe_{1-x}Co_x)_2As_2$. AFM, antiferromagnetic. **b**, Resistivity as a function of temperature for the $x = 0.042$ composition. Blue vertical lines indicate the locations of the various phase transitions. **c**,**d**, Resistive signature of the superconducting transition in the $x = 0.042$ composition as a function of temperature under different amounts of applied uniaxial tensile (**c**) and compressive (**d**) stress. **e**,**f**, Same as in **c** and **d** with resistivity on a log scale.

scale (Fig. 1e,f). At the highest values of ε_{disp}, we measure a non-zero resistivity down to the base temperature of our system.

The broad resistive transition at large values of ε_{disp} raises the question of how to define the phase boundary of the superconducting state. Owing to the extreme sensitivity of T_c to ε_{disp}, even small strain gradients or slight strain drift as the temperature is changing may substantially broaden the transition. To mitigate these effects, we investigated the behaviour of the $x = 0.042$ composition under conditions of fixed temperature and variable ε_{disp}. In addition, in order to confirm that the superconductivity in the bulk of the sample has been suppressed, we also measured the AC magnetic susceptibility as a function of ε_{disp} (Fig. 2a,b), which is a technique already shown to be an effective method for measuring superconducting transitions of strained samples[25,26]. At high temperatures, there is near-zero signal for all ε_{disp}, indicating the sample is in the normal state. Then at low temperatures and low ε_{disp}, there is a diamagnetic signal consistent with a superconducting Meissner screening state. By applying either tensile or compressive stress, this diamagnetic signal is suppressed, and there is a sharp peak in the imaginary part of the signal that we take to be clear evidence of a thermodynamic transition out of the superconducting state. This behaviour mirrors what is seen in the corresponding resistivity data at fixed temperature and variable ε_{disp}, which is shown in Fig. 2c. Current–voltage (I–V) curves performed at fixed temperature and ε_{disp} (Supplementary Fig. 3) reveal suppressed critical currents and nonlinear behaviour near the zero resistivity ($\rho = 0$) phase boundary, and that nonlinearity evolves into linear ohmic behaviour with increasing ε_{disp}, confirming the full recovery of a metallic state.

To further elucidate how the superconducting state responds to the lattice distortion induced by ε_{disp}, we performed X-ray diffraction measurements at beamline 6-ID-B at the Advanced Photon Source where we have a sample environment that can simultaneously measure electrical transport and apply uniaxial stress while performing the X-ray diffraction measurements (see Methods for details). For a finite range of ε_{disp} around zero, both the in-plane and out-of-plane lattice constants do not change as the crystal is being detwinned (Supplementary Fig. 4) as the displacement is being absorbed by shifting domain populations and the orthorhombicity is flat. For higher ε_{disp}, the lattice constants begin to change, and the orthorhombicity $\left(\delta = \frac{a-b}{a+b}\right)$ increases with both compressive and tensile stress. Eventually, at a critical orthorhombicity a finite resistance state is recovered (Fig. 2d). In addition to direct visualization of the evolution of lattice constants, this measurement also demonstrates that the strain within the sample is homogenous by monitoring the sharpness of the Bragg peaks. Overall, the compilation of transport and magnetic susceptibility data for this composition (Fig. 2e) clearly demonstrates a superconductor-to-metal quantum phase transition as a function of ε_{disp}.

The slightly underdoped composition $x = 0.06$ exhibits similar behaviour as the $x = 0.042$ composition (Supplementary Fig. 5). In these underdoped samples the superconducting transition occurs below the antiferromagnetic transition temperature T_N. The application of uniaxial stress increases T_N (refs. [27,28]) (see Methods and Supplementary Fig. 6), hence suppressing spin fluctuations and enhancing static magnetic order, which may also contribute to the suppression of superconductivity. The question arises of whether a natural structural distortion or static magnetic order are necessary ingredients to observe this rapid suppression of T_c. To answer this question, we performed the same resistivity measurements under uniaxial stress on an optimally doped ($x = 0.071$) sample, in which no long-range magnetic order was observed down to T_c. For tetragonal samples, the relevant crystal point group is D_{4h}, and the type of strain induced by uniaxial stress can be decomposed as the sum of two irreducible representations: ε_{A1g}, corresponding to non-symmetry-breaking strains such as volume expansion and

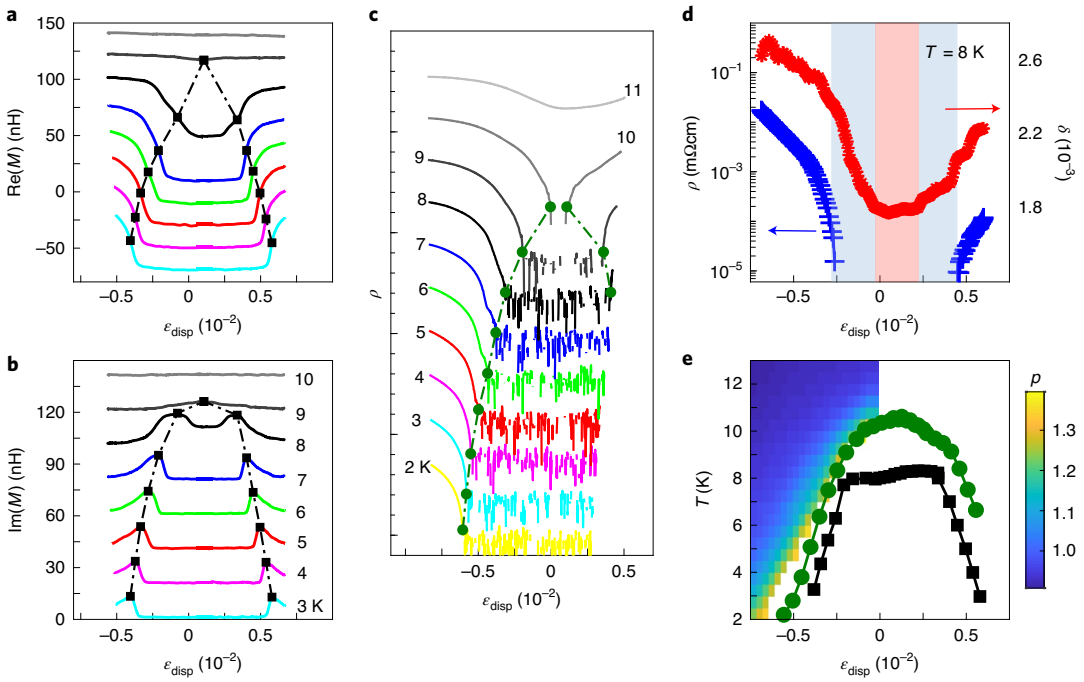

Fig. 2 | Strain-tuned superconductor-to-metal transition in $Ba(Fe_{0.958}Co_{0.042})_2As_2$. a,b, Real (**a**) and imaginary (**b**) parts of the mutual inductance *M* of the susceptometer coils at fixed temperatures. Black squares indicate the strain at which the Meissner effect is suppressed, and curves are offset for clarity. **c**, Resistivity on logarithmic scale under strain at fixed temperatures. Green circles indicate the strain at which the resistivity is non-zero and curves at different temperatures are offset for clarity. **d**, Comparison of the resistivity (blue, log scale) and orthorhombicity (red) during the superconductor-to-metal transition. **e**, Strain–temperature phase diagram for the $x = 0.042$ composition. The black squares indicate the Meissner transition critical values as defined in **b** and green circles indicate the resistive transition critical values as defined in **c**. Colour bar indicates the power *p* of the *I*–*V* characteristic as described in the text.

change of tetragonality, and $\epsilon_{B2g} = \frac{1}{2}\left(\epsilon_{xx} - \epsilon_{yy}\right)$, which breaks the four-fold rotational symmetry. By symmetry considerations, to lowest order the superconducting T_c can only depend quadratically on ε_{B2g} but can depend linearly on ε_{A1g}. Mathematically, we have

$$T_c(\varepsilon) = T_c^0\left(1 + \beta\varepsilon_{A1g} - \frac{1}{2}\alpha\epsilon_{B2g}^2\right)$$

where α and β are the dimensionless coefficients of the dependence of T_c on ε_{A1g} and ε_{B2g} respectively. Consequently, one would expect a monotonic dependence on ε_{disp} if the T_c is primarily determined by ε_{A1g}, and a symmetric response to both positive and negative ε_{disp} if the effect of ε_{B2g} dominates. Remarkably, in the optimally doped sample we observe a strong suppression of superconductivity for both positive and negative ε_{disp}—a nearly fivefold reduction of T_c at about 1% ε_{disp} (Fig. 3a). Although the effect of strain on superconductivity was inferred in several previous works[28,29], here we unambiguously demonstrate the dominant effect of ε_{B2g}. We note that there is no sign of long-range magnetic order induced by strain from resistivity measurements (see Methods and Supplementary Fig. 7). In this situation, ε_{B2g} is expected to enhance spin fluctuations while suppressing nematic fluctuations, as has been previously observed in underdoped samples by nuclear magnetic resonance experiments[18]. Thus, the extreme sensitivity of T_c to B_{2g} strain in the paramagnetic optimally doped sample confirms the role played by the nematic fluctuations in the superconducting pairing.

This extreme sensitivity of the superconducting state to B_{2g} strain is truncated past optimal doping (Fig. 3a); for a slightly overdoped sample with a similar transition temperature ($x = 0.088$), 0.5% of ε_{disp} induced by compressive stress only reduces T_c by 12%, compared with a 50% reduction in the optimally doped sample for the same ε_{disp}. Further into the overdoped regime, ($x = 0.113$) the response of T_c to ε_{disp} is even smaller in magnitude and no longer symmetric for tensile and compressive stress. By calculating the amount of ε_{B2g} at a given ε_{disp} using linear elasticity theory (see Methods for details) and recent systematic measurements of the elastic constants[30], we plot T_c against the purely antisymmetric ε_{B2g} in Fig. 3b,c. It is clear from the behaviour of T_c that there is a crossover from a strongly quadratic response to strain towards a primarily linear response as the doping level is increased.

The drastically different behaviour between underdoped, optimally doped and overdoped samples is rather intriguing. From the symmetry point of view, the suppression of T_c should be directly proportional to the square of the amount of static nematic order induced by a fixed amount of ε_{B2g}, which is measured by the nematic susceptibility. Therefore, we expect a stronger doping dependence of the strain sensitivity of T_c than the nematic susceptibility. In Fig. 3d we plot the doping dependence of the elastoresistivity coefficient $-2m_{66}$ measured just above T_c, which is proportional to the nematic susceptibility, and the strain sensitivity of T_c, characterized by the coefficient α as defined above. The coefficient α indeed shows a much stronger doping dependence compared with $-2m_{66}$. We note that static and/or fluctuating antiferromagnetic order may play a non-trivial role in the determination of α. A systematic study of the strain dependence of spin fluctuations in the overdoped and optimally doped compounds will further quantitatively determine the contribution to superconducting pairing from different degrees of freedom.

In a broader view, regardless of the exact mechanism at play here, these measurements reveal an unprecedented tunability of T_c by lattice deformation in a bulk superconductor. To put iron pnictides into context, we plot in Fig. 4a the normalized maximum change of

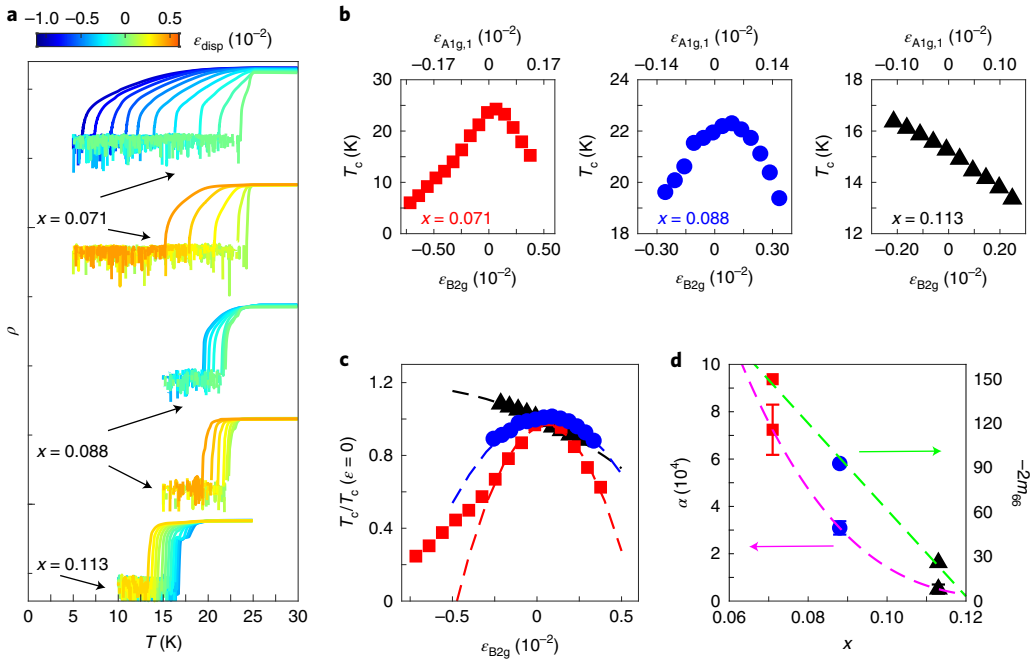

Fig. 3 | Strained superconducting transition of optimally and overdoped $Ba(Fe_{1-x}Co_x)_2As_2$. a, Resistivity as a function of temperature under uniaxial stress for optimally and overdoped compositions plotted in log scale and sets of curves that overlap are offset for clarity. **b**, Extracted superconducting T_c as a function of the two irreducible strain components ε_{B2g} (bottom axis) and $\varepsilon_{A1g,1}$ (top axis). **c**, T_c normalized by the zero-strain value as a function of the purely B_{2g} strain component for all three compositions. Dotted lines are second-order polynomial fits to the low strain data (fit parameters are tabulated in Supplementary Table 2). **d**, Doping dependence of the nematic susceptibility $-2m_{66}$ at $T = 30$ K (right) and normalized quadratic coefficient $\alpha = \frac{-d^2T_c}{d\varepsilon^2}\frac{1}{T_c^0}$ (left). Green and magenta dotted lines are guides to the eye. The error bars for α are defined by the 95% confidence interval for the polynomial fit. The error bars for the nematic susceptibilities are smaller than the size of the data markers.

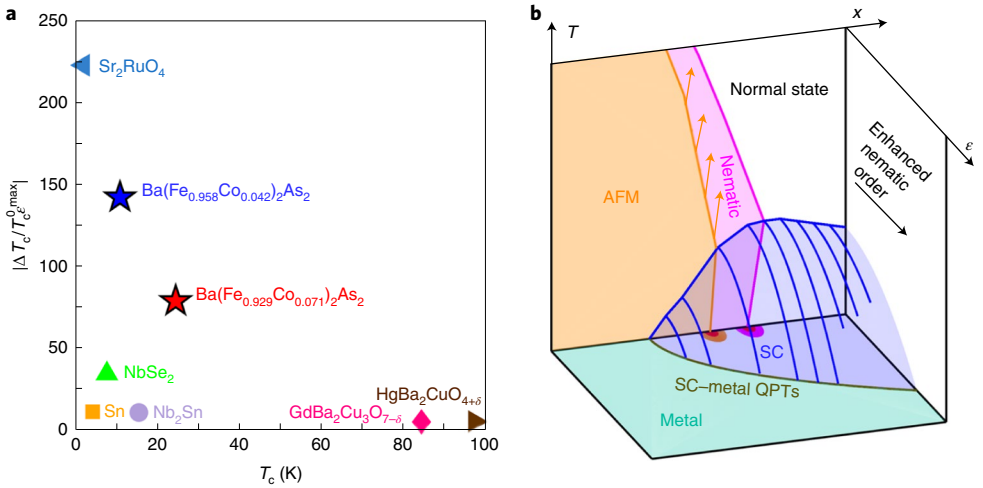

Fig. 4 | Strain tunability of superconducting T_c in $Ba(Fe_{1-x}Co_x)_2As_2$. a, Sensitivity of T_c to strain for a variety of superconductors. The quantity plotted on the vertical axis is the maximum change in T_c as a result of mechanical strain divided by the strain needed to achieve that change and normalized by the zero-strain T_c. The data plotted as well as the references are tabulated in Supplementary Table 3. **b**, Schematic doping–strain–temperature (x–ε–T) phase diagram. The magenta region indicates the electronic nematic phase that breaks the C_4 rotational symmetry, ending in a quantum critical point inside the superconducting (SC) dome (blue region). The orange region indicates the static antiferromagnetic (AFM) order that is enhanced by anisotropic strain for underdoped samples (orange arrows) and that also ends in a putative quantum critical point. At fixed doping, anisotropic strain that enhances the broken symmetry suppresses the superconducting T_c (solid blue lines), generating another superconducting dome tuned by strain instead of doping. The closing of this dome gives way to a metallic phase (green region) and generates a line of strain-tuned superconductor-to-metal quantum phase transitions (SC–metal QPTs) in the x–ε plane (dark green line).

T_c as a result of mechanical strain $\left(\Delta T_c/T_c^0\varepsilon^{max}\right)$ for a diverse group of both conventional and unconventional superconductors[26,31–35]. The normalized sensitivity of the underdoped and optimally doped samples studied in this work is much larger than any other known superconductor other than Sr_2RuO_4. Such tunability allows us to construct the doping–strain–temperature (x–ε–T) phase

diagram shown schematically in Fig. 4b. For a broad range of doping near the composition-tuned nematic quantum critical point, the superconducting state is extremely sensitive to B_{2g} strain that acts to close the superconducting dome in the ε–T plane, generating a line of superconductor–metal quantum phase transitions in the zero-temperature limit.

The superconductor-to-metal (or insulator) transition is one of the most studied quantum phase transitions in condensed-matter physics[36,37]. Nevertheless, previous experimental studies have been mostly restricted to two-dimensional systems, possibly due to the ease of continuous tuning of T_c in thin films or exfoliated thin flakes. Our work presents a new platform to study the superconductor-to-metal transition in a three-dimensional crystal with an in situ tunable strain. The three-dimensional sample may allow experimental probes that were previously inaccessible in a two-dimensional system, such as thermodynamic measurement, which may shed new light onto the recently proposed 'anomalous metal' state[38].

Online content

Any methods, additional references, Nature Research reporting summaries, source data, extended data, supplementary information, acknowledgements, peer review information; details of author contributions and competing interests; and statements of data and code availability are available at https://doi.org/10.1038/s41567-020-0983-9.

Received: 13 January 2020; Accepted: 26 June 2020;
Published online: 10 August 2020

References

1. Gegenwart, P., Si, Q. & Steglich, F. Quantum criticality in heavy-fermion metals. *Nature* **4**, 186–197 (2008).
2. Stewart, G. R. Heavy-fermion systems. *Rev. Mod. Phys.* **56**, 755–787 (1984).
3. Han, G. H., Duong, D. L., Keum, D. H., Yun, S. J. & Lee, Y. H. van der Waals metallic transition metal dichalcogenides. *Chem. Rev.* **118**, 6297–6336 (2018).
4. Manzeli, S., Ovchinnikov, D., Pasquier, D., Yazyev, O. V. & Kis, A. 2D transition metal dichalcogenides. *Nat. Rev. Mater.* **2**, 17033 (2017).
5. Singleton, J. & Mielke, C. Quasi-two-dimensional organic superconductors: a review. *Contemp. Phys.* **43**, 63–96 (2002).
6. Si, Q., Yu, R. & Abrahams, E. High-temperature superconductivity in iron pnictides and chalcogenides. *Nat. Rev. Mater.* **1**, 16017 (2016).
7. Stewart, G. R. Superconductivity in iron compounds. *Rev. Mod. Phys.* **83**, 1589–1641 (2011).
8. Norman, M. R. The challenge of unconventional superconductivity. *Science* **332**, 196–200 (2011).
9. Monthoux, P., Pines, D. & Lonzarich, G. G. Superconductivity without phonons. *Nature* **450**, 1177–1182 (2007).
10. Fradkin, E., Kivelson, S. A., Lawler, M. J., Eisenstein, J. P. & Mackenzie, A. P. Nematic Fermi fluids in condensed matter physics. *Annu. Rev. Condens. Matter Phys.* **1**, 153–178 (2010).
11. Chu, J.-H., Analytis, J. G., Kucharczyk, C. & Fisher, I. R. Determination of the phase diagram of the electron-doped superconductor $Ba(Fe_{1-x}Co_x)_2As_2$. *Phys. Rev. B* **79**, 014506 (2009).
12. Ni, N. et al. Effects of Co substitution on thermodynamic and transport properties and anisotropic H_{c2} in $Ba(Fe_{1-x}Co_x)_2As_2$ single crystals. *Phys. Rev. B* **78**, 214515 (2008).
13. Chubukov, A. V., Fernandes, R. M. & Schmalian, J. Origin of nematic order in FeSe. *Phys. Rev. B* **91**, 201105 (2015).
14. Singh, U. R. et al. Evidence for orbital order and its relation to superconductivity in $FeSe_{0.4}Te_{0.6}$. *Sci. Adv.* **1**, e1500206 (2015).
15. Nandi, S. et al. Anomalous suppression of the orthorhombic lattice distortion in superconducting $Ba(Fe_{1-x}Co_x)_2As_2$ single crystals. *Phys. Rev. Lett.* **104**, 057006 (2010).
16. Hosoi, S. et al. Nematic quantum critical point without magnetism in $FeSe_{1-x}S_x$ superconductors. *Proc. Natl Acad. Sci. USA* **113**, 8139–8143 (2016).
17. Watson, M. D. et al. Emergence of the nematic electronic state in FeSe. *Phys. Rev. B* **91**, 155106 (2015).
18. Kissikov, T. et al. Uniaxial strain control of spin-polarization in multicomponent nematic order of $BaFe_2As_2$. *Nat. Commun.* **9**, 1058 (2018).
19. Mirri, C. et al. Origin of the resistive anisotropy in the electronic nematic phase of $BaFe_2As_2$ revealed by optical spectroscopy. *Phys. Rev. Lett.* **115**, 107001 (2015).
20. Chu, J.-H., Kuo, H.-H., Analytis, J. G. & Fisher, I. R. Divergent nematic susceptibility in an iron arsenide superconductor. *Science* **337**, 710–712 (2012).
21. Kuo, H.-H., Chu, J.-H., Palmstrom, J. C., Kivelson, S. A. & Fisher, I. R. Ubiquitous signatures of nematic quantum criticality in optimally doped Fe-based superconductors. *Science* **352**, 958–962 (2016).
22. Hicks, C. W., Barber, M. E., Edkins, S. D., Brodsky, D. O. & Mackenzie, A. P. Piezoelectric-based apparatus for strain tuning. *Rev. Sci. Instrum.* **85**, 065003 (2014).
23. Chu, J.-H. et al. In-plane resistivity anisotropy in an underdoped iron arsenide superconductor. *Science* **329**, 824–826 (2010).
24. Schmidt, J. et al. Nematicity in the superconducting mixed state of strain detwinned underdoped $Ba(Fe_{1-x}Co_x)_2As_2$. *Phys. Rev. B* **99**, 064515 (2019).
25. Hicks, C. W. et al. Strong increase of T_c of Sr_2RuO_4 under both tensile and compressive strain. *Science* **344**, 283–285 (2014).
26. Steppke, A. et al. Strong peak in T_c of Sr_2RuO_4 under uniaxial pressure. *Science* **355**, eaaf9398 (2017).
27. Tam, D. W. et al. Uniaxial pressure effect on the magnetic ordered moment and transition temperatures in $BaFe_{2-x}T_xAs_2$ (T = Co,Ni). *Phys. Rev. B* **95**, 060505 (2017).
28. Dhital, C. et al. Effect of uniaxial strain on the structural and magnetic phase transitions in $BaFe_2As_2$. *Phys. Rev. Lett.* **108**, 087001 (2012).
29. Kuo, H.-H. et al. Magnetoelastically coupled structural, magnetic, and superconducting order parameters in $BaFe_2(As_{1-x}P_x)_2$. *Phys. Rev. B* **86**, 134507 (2012).
30. Fujii, C. et al. Anisotropic Grüneisen parameter and diverse order parameter fluctuations in iron-based superconductor $Ba(Fe_{1-x}Co_x)_2As_2$. *J. Phys. Soc. Jpn* **87**, 074710 (2018).
31. Wieteska, A. et al. Uniaxial strain tuning of superconductivity in 2H-$NbSe_2$. Preprint at https://arxiv.org/abs/1903.05253 (2019).
32. Kroeger, D. M., Easton, D. S., DasGupta, A., Koch, C. C. & Scarbrough, J. O. The effect of strain upon the scaling law for flux pinning in bronze process Nb_3Sn. *J. Appl. Phys.* **51**, 2184–2192 (1980).
33. Rothberg, B. D., Nabarro, F. R. N., Stephen, M. J. & McLachlan, D. S. in *Low Temperature Physics-LT 13* 528–531 (Springer, 1974).
34. Wang, S. et al. Strain derivatives of T_c in $HgBa_2CuO_{4+\delta}$: the CuO_2 plane alone is not enough. *Phys. Rev. B* **89**, 024515 (2014).
35. Bud'ko, S. L., Guimpel, J., Nakamura, O., Maple, M. B. & Schuller, I. K. Uniaxial pressure dependence of the superconducting critical temperature in $RBa_2Cu_3O_{7-\delta}$ high-T_c oxides. *Phys. Rev. B* **46**, 1257–1260 (1992).
36. Gantmakher, V. F. & Dolgopolov, V. T. Superconductor–insulator quantum phase transition. *Phys. Usp.* **53**, 1–49 (2010).
37. Sondhi, S. L., Girvin, S. M., Carini, J. P. & Shahar, D. Continuous quantum phase transitions. *Rev. Mod. Phys.* **69**, 315–333 (1997).
38. Kapitulnik, A., Kivelson, S. A. & Spivak, B. Colloquium: anomalous metals: failed superconductors. *Rev. Mod. Phys.* **91**, 011002 (2019).

Methods

Sample preparation. Single crystals of $Ba(Fe_{1-x}Co_x)_2As_2$ were grown out of FeAs flux as described previously[11,12]. The crystals preferentially break along the $(100)_{Tet}$ and $(010)_{Tet}$ directions when cleaved, which allowed for determination of the crystallographic directions (the 'Tet' subscript signifies that the Miller indices are referenced from the high-temperature tetragonal lattice). Composition of the samples was determined using energy dispersive spectroscopy. The crystals were cleaved into thin bars with the $(110)_{Tet}$ direction being the longest dimension. Electrical contacts were made in a typical four-point configuration with sputtered gold pads and silver epoxy.

Strain device and strain determination. For applying uniaxial stress, a home-built three-piezo device was used (Supplementary Fig. 1). In this type of strain cell[22], a crystal is glued so that a portion of its length is suspended across a gap in a titanium scaffolding that has three piezo stacks attached in such a way that extension (compression) of the outer stacks and compression (extension) of the inner stack will cause the crystal to experience tensile (compressive) strain. In this configuration, the effect of the thermal expansion of the piezo stacks is greatly reduced because of their symmetric arrangement, and the large ratio of the length of the gap over the length of the piezo stacks allows for large strains of 1% or more to be applied to the sample even at cryogenic temperatures.

Even though the thermal expansion of the piezo stacks is mostly eliminated in this configuration, knowing the displacement of the mounting plates is not enough to know the ε_{disp} experienced by the sample because of two facts. First, the presence of differential thermal contraction between the sample and the titanium from which the plates are made. This requires a separate determination of the zero-strain point on the sample. Second, a non-perfect strain transmission though the epoxy used to affix the sample to the mounting plates.

To address the first point and determine the point of zero strain for the sample, we utilized the fact that the $Ba(Fe_{1-x}Co_x)_2As_2$ system demonstrates relatively large gauge factors, meaning that the resistivity is very sensitive to strain. Thus, to determine zero strain, we would first measure the temperature dependence of the resistivity of a crystal in the free-standing state, not mounted on the strain cell. Then, once mounted on the strain cell, we would sweep the voltage on the stacks until the resistance matched the resistance of the free-standing state just above T_c.

To address the second point, we performed finite-element analysis using the ANSYS Academic Research Mechanical 19.1 software to model the strain transmission utilizing the elastic properties of both the sample, which were taken from ref. [30], and the elastic properties of the mounting epoxy (Loctite Stycast 2850FT), which is available from the manufacturer (Young's modulus $E \sim 15$ GPa, Poisson ratio $\nu \sim 0.3$). The mounting geometry is modelled as two symmetric rectangular slabs of epoxy rigidly bonded to the top and bottom surfaces of the sample on either end of the gap (Supplementary Fig. 2). A fixed displacement is applied to the top and bottom surfaces of each slab of epoxy with a magnitude that would induce 1% strain in the middle of the gap if there were perfect strain transmission. However, because the epoxy deforms upon displacement, not all the applied displacement is transferred to the sample. The result of these calculations is a coefficient μ that indicates the percentage of the strain transmitted to the middle region of the sample, which is the region where we placed the electrical contacts. An example result of the simulation is shown in Supplementary Fig. 2 and the results for all samples measured in the main text are compiled in Supplementary Table 1. Typical values of μ are 0.7–0.9.

Once the zero-point and strain transmission factors are known, monitoring of the strain experienced by the sample was done using a resistive strain gauge. For the resistive strain gauge, the gauge (SS-150–124–15P, Micron Instruments, Simi Valley, CA) is glued onto the back of the centre piezo stack. These gauges have a known room-temperature gauge factor provided by the manufacturer, where the gauge factor g is defined through the equation

$$\Delta\rho/\rho = \frac{\rho(\epsilon) - \rho(\epsilon = 0)}{\rho(\epsilon = 0)} = g \times \epsilon_{piezo}$$

The temperature dependence of the gauge factor was calibrated before the measurements. For this type of strain gauge, $g = 80$ at room temperature and $g = 165$ at our base temperature of 2 K and follows a linear temperature dependence for intermediate temperatures. Here $\epsilon_{piezo} = \frac{\Delta L}{L_{piezo}}$ represents the strain experienced by the piezo itself. Because we always drive the outer piezo stacks exactly opposite to the inner piezo stack, the change of length of the gap across which the sample is suspended is equal to twice the change of length of a single piezo, so we have $\epsilon_{disp} = \mu \frac{2\Delta L}{L_{gap}} = \mu \frac{2 \times L_{piezo}}{L_{gap}} \epsilon_{piezo}$, where μ is the strain transmission factor discussed above. The quantity $\frac{2 \times L_{piezo}}{L_{gap}}$ is the mechanical advantage that allows for large strains to be applied to the sample, and is equal to 36 for typical values of $L_{piezo} = 9$ mm and $L_{gap} = 0.5$ mm. Combining the above equations gives us that the strain experienced by the sample in terms of the strain gauge resistance R^{SG}, which is the quantity that we directly measure, is

$$\epsilon_{disp} = \mu \times \frac{2 \times L_{piezo}}{L_{gap}} \times \frac{R^{SG} - R_0^{SG}}{R_0^{SG}}$$

where R_0^{SG} is the value of the strain gauge resistance at the point where the crystal is in the zero-strain state as determined above.

X-ray diffraction. High-energy X-ray diffraction measurements were performed at beamline 6-ID-B at the Advanced Photon Source with an energy of 11.215 keV and wavelength of 1.10552 Å. The strain cell was mounted on the cold finger of a closed-cycle cryostat allowing for temperature control between 7 and 300 K. Electrical contacts made on the underside of the sample allowed for simultaneous resistivity and diffraction measurements under uniaxial stress without blocking the path of the X-rays. Below the structural/nematic transition, the presence of orthorhombic twin domains causes splitting of the Bragg peaks sensitive to the in-plane lattice constants along the Fe–Fe bonds and uniaxial stress acts to align those domains (Supplementary Fig. 4). By measuring the $(2\ 2\ 12)_{Tet}$, $(1\ -1\ 14)_{Tet}$ and $(0\ 0\ 14)_{Tet}$ Bragg peaks, we were able to extract the orthorhombic a,b in-plane lattice constants both parallel and perpendicular to the direction of applied stress, as well as the out-of-plane c lattice constant. Measurement of the in-plane lattice constant allows for determination of the orthorhombicity $\delta = \frac{a-b}{a+b}$ as a function of applied stress as shown in the main text. In addition, the X-ray diffraction measurements under stress confirm that the crystal is experiencing a state of homogenous strain; the widths of the Bragg peaks under both compressive and tensile strain are comparable to the width of the Bragg peak near zero stress. This, coupled with the fact that we are using a large beam spot (~250 μm) that covers the whole width of the sample, attests to homogenous strains.

Definition and extraction of T_c. Throughout the text, the superconducting T_c is defined as the point where the resistivity of the sample is equal to zero. In the superconducting state, a resistivity measurement made with a lock-in amplifier will yield a signal that consists of a base noise level that is zero on average. One consistent way of defining the point of 'zero resistance' is to find the root mean square of the noise far below the superconducting transition, and then define the transition to zero resistance to be the first point at which the signal falls below that level. This is the definition that we use throughout this work.

The normal state resistivity response to strain. For underdoped samples, strain in the B_{2g} symmetry channel is expected to smear the nematic phase transition at the nematic critical temperature T_s and enhance the magnetic transition temperature T_N. In Supplementary Fig. 6, we show the resistivity and temperature derivative for the $x = 0.042$ composition under different amounts of B_{2g} strain as a function of temperature, and indeed the resistive signature associated with T_s in the free-standing crystal is smeared under finite strain, while T_N is linearly increased. Thus, the magnetic phase boundary is shifted vertically in temperature by ε_{B2g} as shown in Fig. 4b, resulting in suppressed spin fluctuations at $T_c < T_N$. In addition, we show that, as expected, the resistivity anisotropy $(\rho_{xx} - \rho_{yy}) / (\rho_{xx} + \rho_{yy})$ that is proportional to the nematic order parameter is enhanced substantially by ε_{B2g}.

In contrast, for the paramagnetic tetragonal samples, B_{2g} strain is expected to enhance spin fluctuations as long as no static magnetic order develops. In Supplementary Fig. 7, we show the elastoresistive response for the three tetragonal compositions just above T_c, which evolve smoothly as a function of applied strain and show no sign of induced magnetic order. Furthermore, by symmetrizing the data about zero strain, we isolate the response of the average resistivity $(\rho_{xx} + \rho_{yy})$ to ε_{B2g}, which shows a clear quadratic enhancement consistent with an increase of scattering off of spin fluctuations as seen by nuclear magnetic resonance measurements under strain[18]. Our observation of the large quadratic strain sensitivity of T_c near optimal doping in spite of nominally stronger antiferromagnetic fluctuations suggests that nematic fluctuations are indeed contributing substantially to the superconducting pairing.

Relation between applied strain and irreducible strain components. The quantity directly measured in our set-up, ε_{disp}, is the strain along the direction of the current flow, and is not the same as the quantity $\epsilon_{B_{2g}} = \frac{1}{2}(\epsilon_{aa} - \epsilon_{bb})$ that is of the same symmetry as the natural lattice distortion and consequently is the conjugate field that directly couples to the nematic order parameter. In fact, a uniaxial stress applied along one direction will induce strains along all three principal axes. Assuming a tetragonal lattice and letting a and b represent the lengths parallel and perpendicular, respectively, to the direction of strain and c the out-of-plane direction, then we have $\varepsilon_{jj} = -\nu_{ij}\varepsilon_{ii}$, where $\boldsymbol{\nu}_{ij}$ is the appropriate Poisson ratio. This then gives

$$\epsilon_{B_{2g}} = \frac{1}{2}(\epsilon_{aa} - \epsilon_{bb}) = \frac{1}{2}\epsilon_{aa}(1 + \nu_{ab})$$

$$\epsilon_{A1g,1} = \frac{1}{2}(\epsilon_{aa} + \epsilon_{bb}) = \frac{1}{2}\epsilon_{aa}(1 - \nu_{ab})$$

$$\epsilon_{A1g,2} = \epsilon_{cc} = -\epsilon_{aa}\nu_{ac}$$

These are the irreducible representations into which all strains in a crystal with D_{4h} crystal symmetry can be decomposed for the uniaxial type of stress applied

in our experiments. The quantity v_{ij} can be calculated from the coefficients of the compliance tensor. We used detailed temperature and doping dependence[30] of the stiffness tensor of the $Ba(Fe_{1-x}Co_x)_2As_2$ system extracted from ultrasound measurements. However, those coefficients are in the basis of the tetragonal lattice. For a tetragonal crystal, the stiffness tensor takes the form

$$C = \begin{pmatrix} C_{11} & C_{12} & C_{13} & 0 & 0 & 0 \\ C_{12} & C_{11} & C_{13} & 0 & 0 & 0 \\ C_{13} & C_{13} & C_{33} & 0 & 0 & 0 \\ 0 & 0 & 0 & C_{44} & 0 & 0 \\ 0 & 0 & 0 & 0 & C_{44} & 0 \\ 0 & 0 & 0 & 0 & 0 & C_{66} \end{pmatrix}$$

The compliance tensor is the inverse of the stiffness tensor, so we have

$$S = C^{-1} = \begin{pmatrix} \frac{-C_{13}^2+C_{11}C_{33}}{A} & \frac{-C_{13}^2-C_{12}C_{33}}{A} & \frac{C_{13}}{B^+} & 0 & 0 & 0 \\ \frac{-C_{13}^2-C_{12}C_{33}}{A} & \frac{-C_{13}^2+C_{11}C_{33}}{A} & \frac{C_{13}}{B^+} & 0 & 0 & 0 \\ \frac{C_{13}}{B^+} & \frac{C_{13}}{B^+} & \frac{C_{13}}{B^-} & 0 & 0 & 0 \\ 0 & 0 & 0 & \frac{1}{C_{44}} & 0 & 0 \\ 0 & 0 & 0 & 0 & \frac{1}{C_{44}} & 0 \\ 0 & 0 & 0 & 0 & 0 & \frac{1}{C_{66}} \end{pmatrix}$$

where $A = \frac{-C_{13}^2+C_{11}C_{33}}{(C_{11}-C_{12})\left(-2C_{13}^2+C_{33}(C_{11}+C_{12})\right)}$ and $B^{\pm} = \pm\left(2C_{13}^2 - C_{33}(C_{11}+C_{12})\right)$.

This matrix is still in the basis of the tetragonal lattice, whereas we need the matrix in the basis where the in-plane axes are rotated 45° with respect to this basis. We then have

$S' = K^{-T}SK^{-1}$, where K is the rotation matrix given by

$$K = \begin{pmatrix} c^2 & c^2 & 0 & 0 & 0 & 2cs \\ c^2 & c^2 & 0 & 0 & 0 & -2cs \\ 0 & 0 & 1 & 0 & 0 & 0 \\ 0 & 0 & 0 & c & s & 0 \\ 0 & 0 & 0 & -s & c & 0 \\ -cs & cs & 0 & 0 & 0 & c^2-s^2 \end{pmatrix}$$

and $c = \cos(45°)$, $s = \sin(45°)$.

This then gives the rotated compliance tensor:

$$S' = \begin{pmatrix} \frac{C_{33}}{-2B^-} + \frac{1}{4C_{66}} & \frac{C_{33}}{-2B^-} - \frac{1}{4C_{66}} & \frac{C_{13}}{B^+} & 0 & 0 & 0 \\ \frac{C_{33}}{-2B^-} - \frac{1}{4C_{66}} & \frac{C_{33}}{-2B^-} + \frac{1}{4C_{66}} & \frac{C_{13}}{B^+} & 0 & 0 & 0 \\ \frac{C_{13}}{B^+} & \frac{C_{13}}{B^+} & \frac{C_{11}+C_{12}}{B^-} & 0 & 0 & 0 \\ 0 & 0 & 0 & \frac{1}{2C_{44}} & 0 & 0 \\ 0 & 0 & 0 & 0 & \frac{1}{2C_{44}} & 0 \\ 0 & 0 & 0 & 0 & 0 & \frac{2}{C_{11}-C_{12}} \end{pmatrix}$$

Finally, the Poisson ratios of interest $\nu_{ab} = -\frac{\epsilon_{bb}}{\epsilon_{aa}}$ and $\nu_{ac} = -\frac{\epsilon_{cc}}{\epsilon_{aa}}$ are then equal to

$$\nu_{ab} = -\frac{\epsilon_{bb}}{\epsilon_{aa}} = \frac{-S'_{12}}{S'_{11}} = \frac{-C_{13}^2 + \frac{1}{2}(C_{11}+C_{12})C_{33} - C_{33}C_{66}}{-C_{13}^2 + \frac{1}{2}(C_{11}+C_{12})C_{33} + C_{33}C_{66}}$$

$$\nu_{ac} = -\frac{\epsilon_{cc}}{\epsilon_{aa}} = \frac{-S'_{13}}{S'_{11}} = \frac{2C_{13}C_{66}}{-C_{13}^2 + \frac{1}{2}(C_{11}+C_{12})C_{33} - C_{33}C_{66}}$$

The calculated Poisson ratios for the three tetragonal samples are tabulated in Supplementary Table 2.

Data availability

The data that support the plots within this paper and other findings of this study are available from the corresponding author upon reasonable request. Source data are provided with this paper.

Acknowledgements

We thank X. Xu, D. Cobden, B. Spivak, S. Kivelson and C. Xu for discussions. This work was mainly supported by NSF MRSEC at UW (DMR-1719797) and the Gordon and Betty Moore Foundation's EPiQS Initiative, grant GBMF6759 to J.-H.C. The development of strain instrumentation is supported as part of Programmable Quantum Materials, an Energy Frontier Research Center funded by the US Department of Energy (DOE), Office of Science, Basic Energy Sciences (BES), under award DE-SC0019443. The integration of X-ray diffraction with in situ strain is supported by the Air Force Office of Scientific Research Young Investigator Program under grant FA9550-17-1-0217 and the Defense University Research Instrumentation Program Award FA9550-19-1-0180. J.L. acknowledges support from the National Science Foundation under grant no. DMR-1848269. J.-H.C. acknowledges the support of the David and Lucile Packard Foundation and the State of Washington funded Clean Energy Institute.

Author contributions

P.M., J.S., J.M., Q.J. and Z.L. grew the samples. P.M., Q.J. and J.S. did the experiments. P.R., J.-W.K. and J.L. helped conceive and design the X-ray diffraction measurements at the Advanced Photon Source. P.W. performed the finite-element analysis. P.M. analysed the data. J.-H.C. supervised the project. All authors contributed extensively to the interpretation of the data and the writing of the manuscript.

Competing interests

The authors declare no competing interests.

Additional information

Supplementary information is available for this paper at https://doi.org/10.1038/s41567-020-0983-9.

Correspondence and requests for materials should be addressed to J.-H.C.

Peer review information *Nature Physics* thanks Samuel Lederer, Takasada Shibauchi and the other, anonymous, reviewer(s) for their contribution to the peer review of this work.

Reprints and permissions information is available at www.nature.com/reprints.